

Localized topological states beyond Fano resonances via counter-propagating wave mode conversion in piezoelectric microelectromechanical devices

Received: 22 June 2024

Accepted: 28 October 2024

Published online: 07 November 2024

 Check for updates

Jacopo M. De Ponti¹, Xuanyi Zhao², Luca Iorio¹, Tommaso Maggioli², Marco Colangelo², Benyamin Davaji², Raffaele Ardito¹, Richard V. Craster^{3,4} & Cristian Cassella²✉

A variety of scientific fields like proteomics and spintronics have created a new demand for on-chip devices capable of sensing parameters localized within a few tens of micrometers. Nano and microelectromechanical systems (NEMS/MEMS) are extensively employed for monitoring parameters that exert uniform forces over hundreds of micrometers or more, such as acceleration, pressure, and magnetic fields. However, they can show significantly degraded sensing performance when targeting more localized parameters, like the mass of a single cell. To address this challenge, we present a MEMS device that leverages the destructive interference of two topological radiofrequency (RF) counter-propagating wave modes along a piezoelectric Aluminum Scandium Nitride (AlScN) Su-Schrieffer-Heeger (SSH) interface. The reported MEMS device opens up opportunities for further purposes, including achieving more stable frequency sources for communication and timing applications.

Emerging needs in proteomics have created a necessity to sense parameters localized within a few tens of micrometers or less. This is crucial for studying biological processes at a single-cell scale^{1–7}, identifying protein biomarkers associated with specific diseases^{8–12}, achieving atomic-scale resolutions in mass spectrometry^{13–19}, and more; similar needs have emerged even in other fields of study²⁰. For instance, being able to sense spin waves transduced in strongly localized regions²¹ can lead to higher bit densities and improved energy efficiency in high-frequency spintronic memory devices. Similarly, highly localized acoustic modes of vibration in piezoelectric films can provide a path toward robust Quantum State Transfer (QST) between remote superconducting qubits²² and their successful read-out.

Over the past fifteen years, nano and microelectromechanical systems (NEMS/MEMS) have been extensively utilized for sensing parameters (magnetic field^{23–25}, acceleration^{26–29}, pressure^{30–36}, etc.)

that exert nearly uniform forces across hundreds of micrometers along their frequency-setting dimension. However, these devices are significantly limited in their ability to monitor parameters localized within a few tens of micrometers or less (i.e., in their ability to achieve a high “spatial sensing resolution”). In fact, to enable high responsivity in such scenarios, the size of NEMS/MEMS must be shrunk to confine their mode of vibration within an area matching closely the one where the targeted parameter exerts its force. However, shrinking the size of the current MEMS/NEMS, particularly along their frequency-setting dimension, results in a notable reduction of their quality factor (Q) and dynamic range¹⁴, which inevitably impacts the achievable sensing performance³⁷.

Several physical phenomena have been exploited to enhance the spatial sensing resolution of NEMS/MEMS while preserving a high-quality factor. These include internal-resonance^{38–40}, phase-

¹Department of Civil and Environmental Engineering, Politecnico di Milano, Milano, Italy. ²Department of Electrical and Computer Engineering, Northeastern University, Boston, US. ³Department of Mathematics, Imperial College London, London, UK. ⁴Department of Mechanical Engineering, Imperial College London, London, UK. ✉e-mail: c.cassella@northeastern.edu

synchronization^{41–43}, phonon-cavity^{44–47}, and mode-localization^{48–50}. Most of these phenomena originate from the nonlinear interaction between multiple mechanical modes. As a result, they necessitate precise control of these modes' driving conditions. Harnessing these phenomena also requires the use of amplitude read-out schemes, which are inherently more susceptible to accuracy degradations caused by electrical noise than the frequency read-out schemes typically used for linear NEMS/MEMS⁵¹.

In this Article, we demonstrate that both a strong mode-localization and a high-quality factor can be simultaneously achieved in a MEMS device operating in a linear regime by leveraging the destructive interference of two topologically protected states. This interference is achieved by leveraging a unique design strategy based on the creation of a SSH interface supporting counter-propagating symmetric S_0 and antisymmetric A_0 Lamb waves⁵². The counter-propagation of the S_0 and A_0 waves is key to the ultimate high Q factors we obtain and is achieved along the topological SSH interface by breaking the spatial symmetry of an elastic layer, i.e. by corrugating the upper surface of the AlScN layer. This creates two localized states in a one-dimensional wave propagation problem but without using

in-plane symmetry breaking which would be the usual approach to create topological states in acoustics or elasticity^{53,54}. These states, from now on labeled *State-1* and *State-2* (Fig. 1a), show comparable lifetimes. Also, they are both localized around an interface, which marks a significant difference between the dark and bright states (Fig. 1b) forming a Fano resonance (i.e. the bright state approaches a continuum state and the dark state is a localized state)^{55,56}.

The interference between *State-1* and *State-2* is described by coupling counter-propagating symmetric S_0 and antisymmetric A_0 Lamb waves⁵² at a topological interface in an elastic waveguide (Fig. 1c).

To verify the generation of States-1-2 we have built a MEMS device operating in the radiofrequency range that uses a piezoelectric Aluminum Scandium Nitride (AlScN) layer (Fig. 1e). This device reconstructs an elastic version of the SSH model⁵⁷, where an interface is encountered between two periodic structures referred to as C1 and C1'. The unit cells of each structure shares the same periodicity a , but have corrugated elements separated by Δ and $a - \Delta$, respectively. This creates two topological interface states with distinct Zak phases and different wavenumbers, as shown in the numerically computed dispersion curves reported in Fig. 1d.

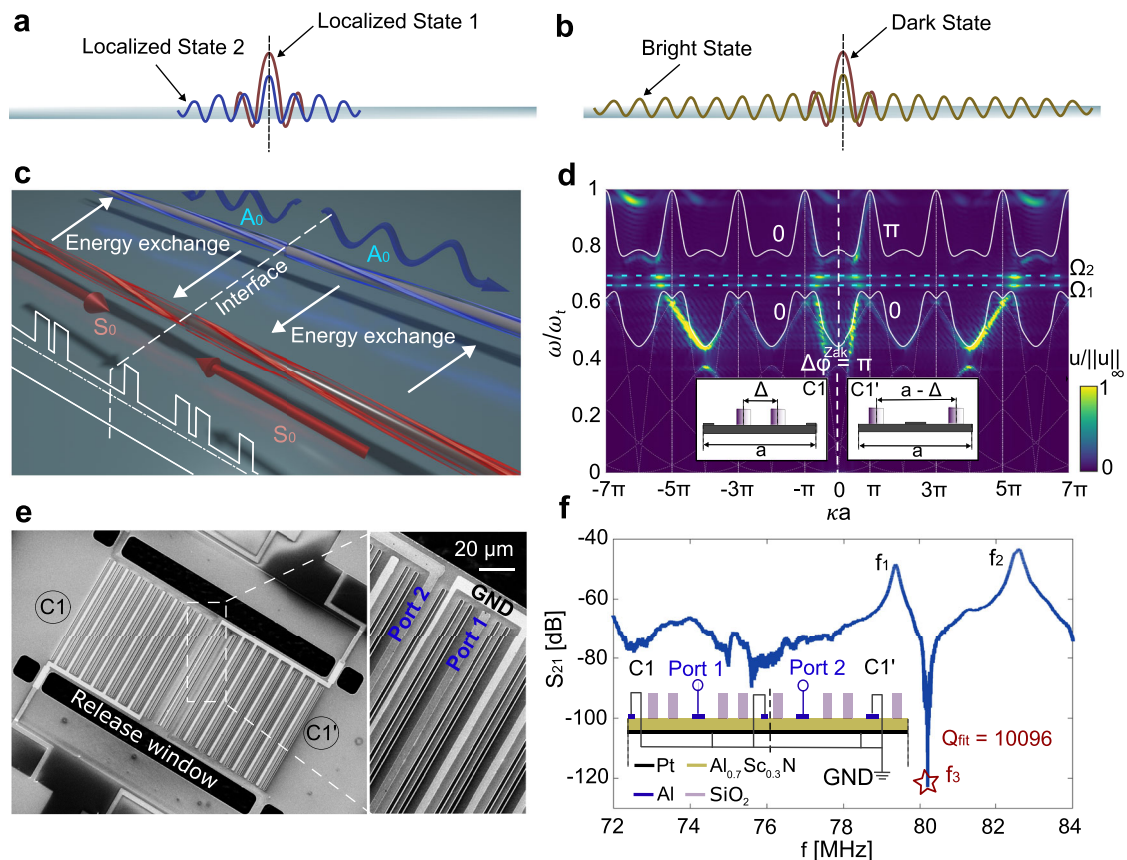


Fig. 1 | Schematic of the physics and the reported MEMS device, aided by theoretical and experimental results. **a** Strong wave localization is achieved by leveraging the interference of two topologically protected localized states, named as *State-1* and *State-2*. **b** This scenario differs from the conventional Fano resonance, wherein the dark and bright states have very different lifetimes, i.e. the bright state approaches a continuum state and the dark mode is a localized state. **c** 3D rendering of the schematized topological problem: the interference between *State-1* and *State-2* is described by coupling, at a topological interface, counter-propagating symmetric (S_0) (red) and antisymmetric (A_0) (blue) Lamb waves each with distinct Zak phases. **d** Such wave coupling is achieved, in one-dimensional wave propagation, by breaking the horizontal spatial symmetry, i.e. by corrugating one side of the surface of an elastic plate. This structure is then combined with an elastic version of the SSH model, where an interface is encountered between two

periodic structures (C1 and C1'). The unit cells of each structure shares the same periodicity a , but have corrugated elements separated by Δ and $a - \Delta$ respectively. This creates two topological interface states with distinct Zak phases and different wavenumbers, as shown by the 2D Fast Fourier Transform of wavefield from numerical simulations. Refer to Table S1 in the supplementary material for a description of all variables included in the plot. **e** We report a piezoelectric MEMS prototype using Aluminum Scandium Nitride as a piezoelectric material, Silicon Oxide to form the periodic corrugations of C1 and C1', and Aluminum strips to form the electrical ports. **f** The experimental electrical transmission of this MEMS device, expressed in terms of the S_{21} scattering parameter, shows the existence of two interface states that lie within a complete bandgap. At their destructive interference, marked with a red star, strong localization is achieved, as well as a record-high Q for MEMS devices using AlScN films as piezoelectric layers.

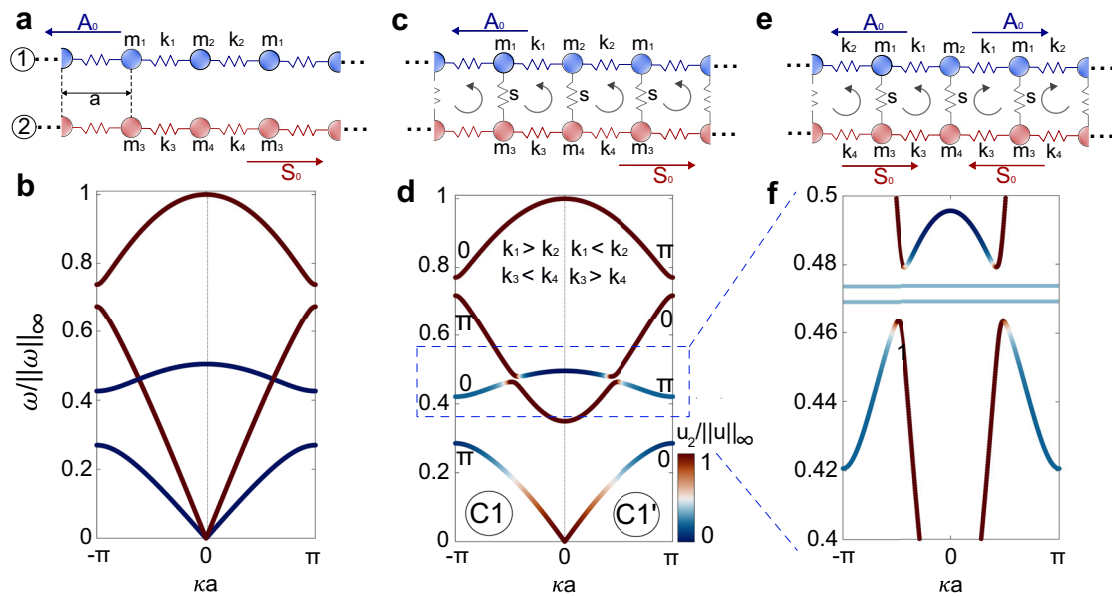


Fig. 2 | The creation of topological interface states via counter-propagating wave mode conversion is analytically described using a spring-mass model. **a** Chain 1 (blue) models the propagation of antisymmetric A_0 waves while chain 2 (red) models the propagation of symmetric S_0 waves. **b** When the chains are disconnected, no coupling occurs and band crossing is observed. **c** The introduction of elastic connections couples the two modes, opening a complete bandgap (**d**) where distinct Zak phases guarantee the existence of non-trivial topological states.

e The introduction of an interface between the initial chain, having stiffness k_1 , k_2 , k_3 , k_4 and its mirrored counterpart, i.e. k_2 , k_1 , k_4 , k_3 , enables two topological states, here demonstrated from a supercell dispersion analysis (**f**). The color map of the dispersion curves shows the relative polarization of the waves, with blue points corresponding to vertical (out-of-plane) polarization, while red refers to horizontal (in-plane) polarization, i.e. A_0 and S_0 waves.

We also show that the interaction between State-1 and State-2 creates an interference state (State-3) even more localized than both State-1 and State-2. In fact, the majority of the energy stored by the device when transducing State-3 is confined within less than $21 \mu\text{m}$ along the frequency setting dimension. The stronger localization of State-3 enables a significant reduction in radiation losses (also known as anchor losses for NEMS/MEMS devices⁵⁸) towards the surrounding silicon substrate. As a result, State-3 exhibits a Q substantially higher than States-1,2.

The Q factor of AlScN resonators is usually affected by various dissipation mechanisms, including thermoelastic damping⁵⁹, interfacial losses⁶⁰, ohmic losses, and anchor losses⁶¹. The anchor losses—caused by acoustic energy leaking into the resonator's surroundings—are dominant when the effective cavity size of AlScN resonators is reduced along the frequency-setting dimension⁶², and this effective size reduction is initially suggestive of similar leakage in the MEMS device reported in this work. Previous studies have attempted to mitigate anchor losses in AlScN resonators by using reflectors^{63,64}, however it is notable that the AlScN device reported here demonstrates a Q at the resonance frequency of State-3 (Fig. 1f) that is five times higher or more than any previously reported device made from a thin AlScN film. An additional advantage of the MEMS device is that States-1-3 exist within a topologically protected bandgap; this provides immunity to the typical defects^{65,66} relaxing required tolerances for the microfabrication of chip-scale devices.

Results

The MEMS device demonstrated in this study consists of two periodic structures (i.e., C1 and C1') formed by SiO_2 grooves deposited atop a suspended thin bilayer plate. This plate embodies a piezoelectric AlScN layer and a platinum (Pt) layer. C1 and C1' have the same pitch of the unit cell (a) but the position of their SiO_2 grooves is shifted by an amount equal to Δ and $a - \Delta$ respectively, as shown in the inset of Fig. 1d. This allows us to synthesize an elastic version of the SSH-model. Two 100 nm-thick Al metallic strips are used to piezoelectrically excite

the device. These strips, each one forming an electrical port (Port-1 or Port-2), have been positioned near the interface of C1 and C1' to ensure strong enough piezoelectric transduction efficiency to successfully validate the presence of States-1-3 from the extraction of the device's electrical scattering parameters (i.e., the S-parameters). Other grounded Al strips have been inserted across the device to preserve the same dispersion characteristics for all unit cells. Four anchors are used to support the fabricated device after its structural release (i.e., after the removal of the silicon underneath the device to generate a suspension). A Scanned Electron Microscope (SEM) picture of the fabricated device is reported in Fig. 1e while the device's electrical transmission (i.e., its S_{21} scattering parameter) is anticipated in Fig. 1f.

The physics of the S_0 - A_0 counter-propagating wave mode conversion in the reported AlScN device can be conceptually idealized by coupling two distinct elastic waveguides supporting S_0 and A_0 wave modes, as usually done to describe wave locking⁶⁷ (Fig. 1c). Both waveguides can be modeled as independent periodic chains (Fig. 2a) including a set of masses and springs (i.e., m_1 , m_2 , k_1 , k_2 and m_3 , m_4 , k_3 , k_4 respectively). These chains mimic the propagation of the A_0 and S_0 wave modes when no coupling between them occurs. The solution to the wave-equation for the system in Fig. 2a can be found by solving the time-independent Schrödinger equation for any possible Bloch state:

$$\hat{H}_{\kappa}|\Psi_{k\kappa n}\rangle = E_{k\kappa n}|\Psi_{k\kappa n}\rangle. \quad (1)$$

In Eq. (1), $E_{k\kappa n}$ identifies a time-independent eigenvalue relative to the wavevector κ for a specific propagating n th mode. Similarly, $|\Psi_{k\kappa n}\rangle$ denotes the solution to the wave-equation for the n th mode and wavevector κ .

The solution of Eq. (1) for the independent chains in Fig. 2a is reported in Fig. 2b in terms of dispersion curves relating frequency and wavenumber. In order to model the coupling between the A_0 wave and the S_0 wave in our structure, we add connecting springs between the

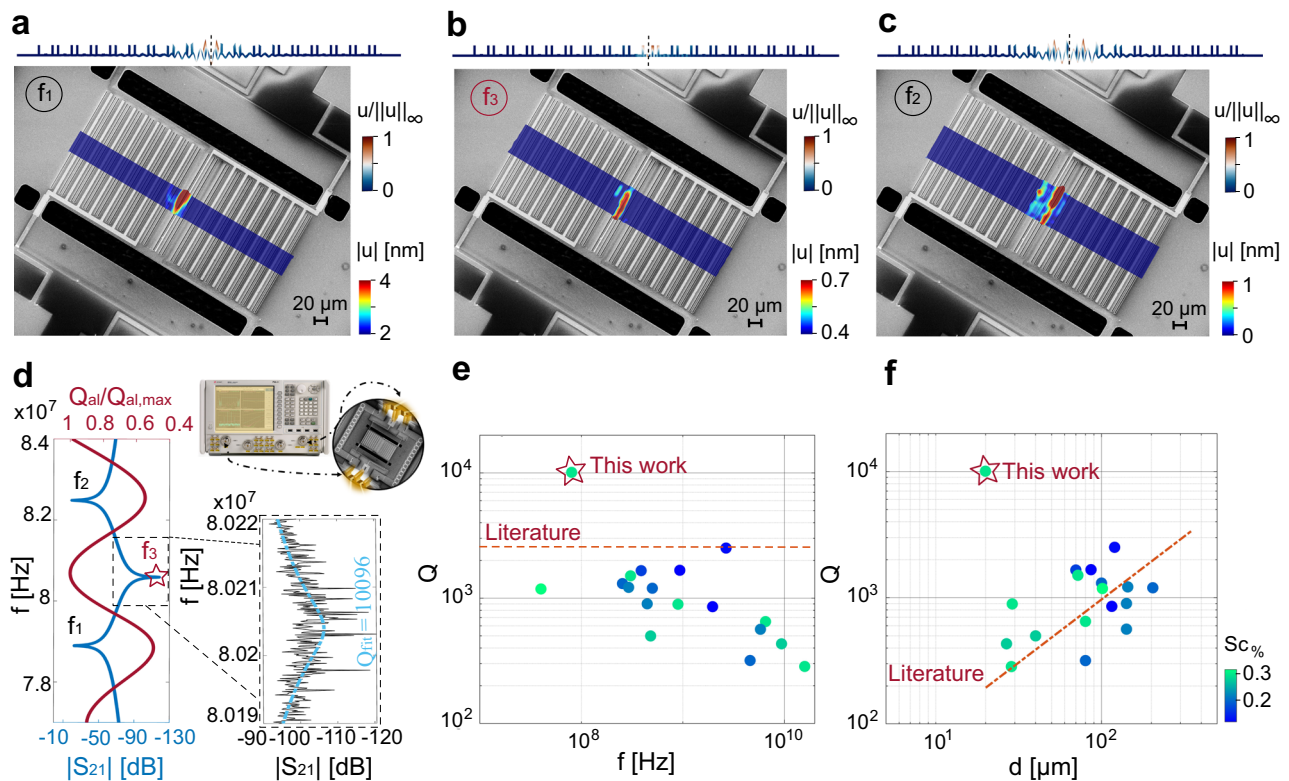


Fig. 3 | Experimental displacement field and Q factor of the reported MEMS device. Measured displacement magnitude for the midsection of the reported MEMS device when operating at f_1 (a), f_2 (b) and f_3 (c). The measurements were performed through a high-frequency vibrometer. Also, corresponding FEM simulated cross-sectional displacement modeshapes are reported above each one of these measured plots. **d** The fabricated MEMS device was electrically tested by probing its input and output ports through two RF GSG probes and by using a Vector Network Analyzer (VNA). We report the FEM calculated frequency distribution of the device transmission (S_{21} , in blue), together with a trend of the normalized quality factor term associated to anchor losses (in red) vs. frequency.

Also, a zoomed-in picture of the measured S_{21} around f_3 is also reported, together with the analytical fitting line we have generated to quantify the MEMS device's Q at f_3 . **e** A comparison of the Q achieved by the reported MEMS device (see the red star) with those previously reported by state-of-the-art AlScN devices. **f** The same pool of devices has been also used to analyze the Q attained by our reported device vs. the size of its resonant cavity (i.e., d) with the corresponding values for each previously reported resonator listed in **e**. Evidently, the MEMS device reported in this work not only shows a superior quality factor, but also demonstrates the capability of overruling the current strict correlation of Q with the effective size of the resonant cavity in AlScN MEMS devices.

two chains, as shown in Fig. 2c. The resulting dispersion curves are reported in Fig. 2d, where a complete bandgap appears due to the coupling of the two modes. The full \hat{H} matrix, its perturbation and the model parameters for the case study described in Fig. 2 are reported in the analytical section of the Supplementary Material.

Next, we can look at the case where an SSH model is reconstructed from the two chains described in Fig. 2a, c. To do so, we connect each chain in Fig. 2c with a mirrored version forming the CI' structure (Fig. 2e). The calculation of the Zak phase⁶⁸ for both CI and CI' allows us to verify that non trivial interface states localized at the common interface exist, and these states are topologically protected, being the bandgaps of CI and CI' endowed with distinct Zak phases. Details about this calculation are reported in the analytical section of the Supplementary Material. The dispersion curves of the supercell, reported in Fig. 2f for the system shown in Fig. 2e clearly demonstrate the existence of two interface states inside the topological bandgap. As both states have mixed polarizations and store their entire elastic energy within few unit cells around the same interface discontinuity, they can interfere. As a result, an interference state arises, as expected (see Fig. S1) from the analysis of the spring-mass chain system shown in Fig. 2e. The modal characteristics of the interference state have been investigated both numerically and experimentally for the MEMS device built in this work, as described in the following.

We characterized the electrical response of the MEMS device demonstrated in this work by measuring its S_{21} transmission from

60 MHz to 110 MHz using a Vector Network Analyzer. The device's S_{21} trend shows two peaks and one notch in its electrical transmission (i.e., in its S_{21}). The two peaks correspond to States-1,2 while the notch corresponds to State-3. From our measured S_{21} vs. frequency trend, we extracted the Q value of State-3. We found the Q of State-3 to be higher than 10,000, as shown in Fig. 1f. We characterized the localization of States-1–3 by direct measurement of the reported device's displacement through a high-frequency vibrometer (Fig. 3a–c). We found the measured displacement for State-3 to be localized within an effective cavity width (d , calculated along the frequency setting dimension) of 21 μm . Such a d value was attained by identifying the width of the region around the interface characterized by displacement magnitudes higher than $\frac{1}{e} \cdot \mu_{max}$, where μ_{max} is the maximum displacement and e is the Neper number. In turn, States-1,2 exhibit a lower Q (approximately 700) and show a more spread modal energy distribution, with State-1 being more localized than State-2. These findings have been confirmed numerically through additional FEM simulations (see in the top insets of Fig. 3a–c the FEM simulated cross-sectional modeshapes of the total displacement for States-1-3).

The strong localization of State-3 allows to obtain an exceptionally high- Q , being the leakage of elastic energy into the surrounding silicon substrate minimized. To confirm this, we simulated the device's response through Finite Element Methods (FEM), extracting its S_{21} trend at various frequencies (see Fig. 3d) as well as the trend of its Q term (Q_{al}) associated to anchor losses. Our FEM simulations

further confirm the presence of States-1,3. Also, they show a significant enhancement in the simulated Q_{at} value for frequencies approaching the resonance frequency of State-3 (f_3), as shown in Fig. 3d.

Discussion

We have demonstrated a topological microacoustic device using a suspended AlScN thin-film. This device leverages the interaction of two interface states with hybrid polarizations and comparable localization properties. This allows us to generate an interference state simultaneously exhibiting a strong mode-localization and a high quality factor. We compare in Fig. 3e the Q achieved at f_3 by the built MEMS device with the Q value of other recent AlScN thin-film MEMS devices operating in the RF range. Evidently, the MEMS device demonstrated in this work shows a quality factor exceeding by more than five times anything reported previously for AlScN MEMS devices. Furthermore, we report in Fig. 3f the trend of the measured Q value vs. the size of the region where the modal energy is confined along the frequency setting dimension (i.e., d) for each one of the AlScN MEMS device reported in Fig. 3e. The d values for all the devices listed in Fig. 3f have been extracted from reported modeshape distributions. Evidently, a reduction in Q typically occurs for devices showing a lower d value. However, the MEMS device reported in this work overcomes this limitation by exhibiting a Q value more than one order of magnitude higher than what reported for AlScN MEMS devices with comparable d values. Due to its record high Q , the MEMS device reported in this work also promises to create a pathway to achieve MEMS sensors with a lower limit-of-detection (LoD). In fact, the minimum LoD of any MEMS/NEMS sensors is constrained by thermomechanical noise-induced fluctuations of their resonance frequency^{37,69,70}. These fluctuations decrease inversely with Q , which underscores the importance of achieving a higher Q in order to improve the achievable LoD. Furthermore, the high- Q achieved by the reported MEMS device at f_3 also creates a path to achieve ultra-stable MEMS-based frequency synthesizers for timing and frequency conversion⁷¹, which can be manufactured with conventional semiconductor processes.

Methods

The fabrication process of the reported MEMS device starts with the deposition of an AlN/Pt/AlScN stack, which is implemented by reactive co-sputtering in the same multi-target chamber, without breaking the vacuum. Then, we etch the AlN/Pt/AlScN stack to form “release windows”. This step is key as it gives direct access to silicon, which is required to be able to etch the silicon under the device through a XeF₂ isotropic etching step (ensuring its suspension). Wet-etching of AlScN is then processed to create vias, allowing to electrically ground the bottom Pt layer. Then we sputter and pattern a 2 μm-thick SiO₂ layer via Plasma-enhanced chemical vapor deposition (PECVD) to form the surface corrugations, which have the longest dimension along the out-of-plane direction (i.e., along the anchors’ direction). Etching of the SiO₂ layer to form the corrugations is implemented through a reactive-ion etching (RIE) step. The Al strips are attained by sputtering and patterning a 150 nm-thick aluminum (Al) layer.

Finally, we deposit a 300 nm-thick gold (Au) layer through evaporation to cover the vias, routing lines and probing pads, ensuring lower ohmic losses. A process flow chart is provided in the supplementary material, together with the definition of the experimental setup.

Data availability

The numerical and experimental data supporting our findings are available, under a Creative Commons Attribution 4.0 International License, on the Zenodo repository as MATLAB figure (.fig) files, accessible at the following <https://doi.org/10.5281/zenodo.13850960>.

References

- Gil-Santos, E. et al. Optomechanical detection of vibration modes of a single bacterium. *Nat. Nanotechnol.* **15**, 469–474 (2020).
- Zajiczek, L. et al. Nano-mechanical single-cell sensing of cell-matrix contacts. *Nanoscale* **8**, 18105–18112 (2016).
- Maloney, N., Lukacs, G., Jensen, J. & Hegner, M. Nanomechanical sensors for single microbial cell growth monitoring. *Nanoscale* **6**, 8242–8249 (2014).
- Grover, W. H. et al. Measuring single-cell density. *Proc. Natl Acad. Sci.* **108**, 10992–10996 (2011).
- Andersson, H. & van den Berg, A. Microtechnologies and nanotechnologies for single-cell analysis. *Curr. Opin. Biotechnol.* **15**, 44–49 (2004).
- Ahmad, M. R., Nakajima, M., Kojima, S., Homma, M. & Fukuda, T. In situ single cell mechanics characterization of yeast cells using nanoneedles inside environmental SEM. *IEEE Trans. Nanotechnol.* **7**, 607–616 (2008).
- Ilic, B. et al. Single cell detection with micromechanical oscillators. *J. Vac. Sci. Technol. B: Microelectron. Nanomater. Struct. Process., Meas. Phenom.* **19**, 2825–2828 (2001).
- Hanay, M. S. et al. Single-protein nanomechanical mass spectrometry in real time. *Nat. Nanotechnol.* **7**, 602–608 (2012).
- Yaari, Z. et al. A perception-based nanosensor platform to detect cancer biomarkers. *Sci. Adv.* **7**, eabj0852 (2021).
- Mao, S., Yu, K., Lu, G. & Chen, J. Highly sensitive protein sensor based on thermally-reduced graphene oxide field-effect transistor. *Nano Res.* **4**, 921–930 (2011).
- Cui, Y., Wei, Q., Park, H. & Lieber, C. M. Nanowire nanosensors for highly sensitive and selective detection of biological and chemical species. *Science* **293**, 1289–1292 (2001).
- Cai, D. et al. A molecular-imprint nanosensor for ultrasensitive detection of proteins. *Nat. Nanotech.* **5**, 597–601 (2010).
- Sansa, M. et al. Optomechanical mass spectrometry. *Nat. Commun.* **11**, 3781 (2020).
- Ekinci, K. L., Yang, Y. T. & Roukes, M. L. Ultimate limits to inertial mass sensing based upon nanoelectromechanical systems. *J. Appl. Phys.* **95**, 2682–2689 (2004).
- Chaste, J. et al. A nanomechanical mass sensor with yoctogram resolution. *Nat. Nanotech.* **7**, 301–304 (2012).
- Gil-Santos, E. et al. Nanomechanical mass sensing and stiffness spectrometry based on two-dimensional vibrations of resonant nanowires. *Nat. Nanotech.* **5**, 641–645 (2010).
- Zobenica, Z. et al. Integrated nano-opto-electro-mechanical sensor for spectrometry and nanometrology. *Nat. Commun.* **8**, 2216 (2017).
- Naik, A. K., Hanay, M. S., Hiebert, W. K., Feng, X. L. & Roukes, M. L. Towards single-molecule nanomechanical mass spectrometry. *Nat. Nanotech.* **4**, 445–450 (2009).
- Thakur, A. K. & Movileanu, L. Real-time measurement of protein-protein interactions at single-molecule resolution using a biological nanopore. *Nat. Biotechnol.* **37**, 96–101 (2019).
- Manenti, R. et al. Quantum acoustics with superconducting qubits. *Nat. Commun.* **8**, 975 (2020).
- Kobayashi, D. et al. Spin current generation using a surface acoustic wave generated via spin-rotation coupling. *Phys. Rev. Lett.* **119**, 077202 (2017).
- Zhang, R., Song, Z.-Y., Liu, W. & Zheng, S.-B. Robust quantum state transfer via topological edge states in superconducting qubit chains. *Phys. Rev. Lett.* **124**, 010505 (2020).
- Nan, T., Hui, Y., Rinaldi, M. & Sun, N. X. Self-biased 215mhz magnetoelectric NEMS resonator for ultra-sensitive DC magnetic field detection. *Sci. Rep.* **3**, 1985 (2013).
- Mbarek, S. B., Alcheikh, N., Ouakad, H. M. & Younis, M. I. Highly sensitive low field Lorentz-force MEMS magnetometer. *Sci. Rep.* **11**, 21634 (2021).

25. Zaeimbashi, M. et al. Ultra-compact dual-band smart NEMS magnetoelectric antennas for simultaneous wireless energy harvesting and magnetic field sensing. *Nat. Commun.* **12**, 3141 (2021).
26. Xu, L., Wang, S., Jiang, Z. & Wei, X. Programmable synchronization enhanced MEMS resonant accelerometer. *Microsyst. Nanoeng.* **6**, 1–10 (2020).
27. Kononchuk, R., Cai, J., Ellis, F., Thevamaran, R. & Kottos, T. Exceptional-point-based accelerometers with enhanced signal-to-noise ratio. *Nature* **607**, 697–702 (2022).
28. Middlemiss, R. P. et al. Measurement of the earth tides with a MEMS gravimeter. *Nature* **531**, 614–617 (2016).
29. Mustafazade, A. et al. A vibrating beam MEMS accelerometer for gravity and seismic measurements. *Sci. Rep.* **10**, 10415 (2020).
30. Morten, B., De Cicco, G. & Prudenziati, M. Resonant pressure sensor based on piezoelectric properties of ferroelectric thick films. *Sens. Actuators A: Phys.* **31**, 153–158 (1992).
31. Welham, C. J., Gardner, J. W. & Greenwood, J. A laterally driven micromachined resonant pressure sensor. *Sens. Actuators A: Phys.* **52**, 86–91 (1996).
32. Li, M., Tang, H. X. & Roukes, M. L. Ultra-sensitive NEMS-based cantilevers for sensing, scanned probe and very high-frequency applications. *Nat. Nanotechnol.* **2**, 114–120 (2007).
33. Venstra, W. J., Capener, M. J. & Elliott, S. R. Nanomechanical gas sensing with nonlinear resonant cantilevers. *Nanotechnology* **25**, 425501 (2014).
34. Li, Y. et al. Thermally stable piezoelectric sensors for quantitative pressure sensing based on linear piezoelectric zinc oxide thin films. *Mater. Des.* **235**, 112466 (2023).
35. Peng, L. et al. A single-side micromachined MPa-scale high-temperature pressure sensor. *Micromachines* **14**, 1–11 (2023).
36. Sadl, M. et al. Construction and functionality of a ceramic resonant pressure sensor for operation at elevated temperatures. *Sensors* **18**, 1–13 (2018).
37. Qian, Z., Rajaram, V., Sungho, K. & Rinaldi, M. High figure-of-merit NEMS thermal detectors based on 50-nm thick AlN nano-plate resonators. *Appl. Phys. Lett.* **115**, 1–5 (2019).
38. Xia, C., Wang, D. F., Ono, T., Itoh, T. & Esashi, M. Internal resonance in coupled oscillators - Part I: A double amplification mass sensing scheme without Duffing nonlinearity. *Mech. Syst. Signal Process.* **159**, 107886 (2021).
39. Wang, X. et al. Frequency comb in 1:3 internal resonance of coupled micromechanical resonators. *Appl. Phys. Lett.* **120**, 173506 (2022).
40. Hajjaj, A. Z., Ruzziconi, L., Alfossail, F. & Theodossiadis, S. Combined internal resonances at crossover of slacked micromachined resonators. *Nonlinear Dyn.* **110**, 2033–2048 (2022).
41. Pu, D. et al. Anomalous amplitude-frequency dependence in a micromechanical resonator under synchronization. *Nonlinear Dyn.* **103**, 467–479 (2021).
42. Xu, L., Qi, Y., Jiang, Z. & Wei, X. Fast frequency relocking for synchronization enhanced resonant accelerometer. *Microsyst. Nanoeng.* **8**, 1–8 (2022).
43. Defoort, M., Hentz, S., Shaw, S. W. & Shoshani, O. Amplitude stabilization in a synchronized nonlinear nanomechanical oscillator. *Commun. Phys.* **5**, 1–7 (2022).
44. Miao, T. et al. Nonlinearity-mediated digitization and amplification in electromechanical phonon-cavity systems. *Nat. Commun.* **13**, 2352 (2022).
45. Asadi, K., Yu, J. & Cho, H. Nonlinear couplings and energy transfers in micro- and nano-mechanical resonators: intermodal coupling, internal resonance and synchronization. *Philos. Trans. A Math. Phys. Eng. Sci.* **376**, 20170141 (2018).
46. Okamoto, H. et al. Coherent phonon manipulation in coupled mechanical resonators. *Nat. Phys.* **9**, 480–484 (2013).
47. Zhao, C. et al. Toward high-resolution inertial sensors employing parametric modulation in coupled micromechanical resonators. *Phys. Rev. Appl.* **12**, 044005 (2019).
48. Spletzer, M., Raman, A., Wu, A. Q., Xu, X. & Reifenberger, R. Ultra-sensitive mass sensing using mode localization in coupled micro-cantilevers. *Appl. Phys. Lett.* **88**, 254102 (2006).
49. Zhao, C. et al. A review on coupled MEMS resonators for sensing applications utilizing mode localization. *Sens. Actuators A: Phys.* **249**, 93–111 (2016).
50. Peng, B. et al. A sensitivity tunable accelerometer based on series-parallel electromechanically coupled resonators using mode localization. *J. Microelectromech. Syst.* **29**, 3–13 (2020).
51. Wang, K. et al. A decouple-decomposition noise analysis model for closed-loop mode-localized tilt sensors. *Microsyst. Nanoeng.* **9**, 1–11 (2023).
52. Lamb, H. On waves in an elastic plate. *Proc. R. Soc. A: Math. Phys. Eng.* **93**, 1–15 (1917).
53. Zangeneh-Nejad, F. & Fleury, R. Topological Fano resonances. *Phys. Rev. Lett.* **122**, 014301 (2019).
54. Zhang, Z.-D., Zhang, X.-M., Yu, S.-Y., Lu, M.-H. & Chen, Y.-F. Tunable topological Fano resonances in graphene-based nanomechanical lattices. *Phys. Rev. Appl.* **18**, 054029 (2022).
55. Miroshnichenko, A. E., Flach, S. & Kivshar, Y. S. Fano resonances in nanoscale structures. *Rev. Mod. Phys.* **82**, 2257–2298 (2010).
56. Limonov, M. F., Rybin, M. V., Poddubny, A. N. & Kivshar, Y. S. Fano resonances in photonics. *Nat. Photonics* **11**, 543–554 (2017).
57. Su, W. P., Schrieffer, J. R. & Heeger, A. J. Solitons in polyacetylene. *Phys. Rev. Lett.* **42**, 1698–1701 (1979).
58. Lee, D., Jahanbani, S., Kramer, J., Lu, R. & Lai, K. Nanoscale imaging of super-high-frequency microelectromechanical resonators with femtometer sensitivity. *Nat. Commun.* **14**, 1–7 (2023).
59. Lifshitz, R. & Roukes, M. L. Thermoelastic damping in micro-and nanomechanical systems. *Phys. Rev. B* **61**, 5600 (2000).
60. Mathew, J. P. et al. Nanoscale electromechanics to measure thermal conductivity, expansion, and interfacial losses. *Nano Lett.* **15**, 7621–7626 (2015).
61. Segovia-Fernandez, J., Cremonesi, M., Cassella, C., Frangi, A. & Piazza, G. Anchor losses in aln contour mode resonators. *J. Microelectromech. Syst.* **24**, 265–275 (2014).
62. Hagelauer, A. et al. From microwave acoustic filters to millimeter-wave operation and new applications. *IEEE J. Microw.* **3**, 484–508 (2023).
63. Lin, C.-M., Hsu, J.-C., Senesky, D. G. & Pisano, A. P. Anchor loss reduction in aln lamb wave resonators using phononic crystal strip tethers. In *2014 IEEE International Frequency Control Symposium (FCS)*, 1–5 (IEEE, 2014).
64. Zhao, X. et al. Extending the linearity of alscn contour-mode resonators through acoustic metamaterials-based reflectors. *IEEE Trans. Ultrason. Ferroelectr. Freq. Control* **70**, 1229–1238 (2023).
65. Moore, J. E. The birth of topological insulators. *Nature* **464**, 194–198 (2010).
66. Huber, S. D. Topological mechanics. *Nat. Phys.* **12**, 621–623 (2016).
67. Mace, B. R. & Manconi, E. Wave motion and dispersion phenomena: Veering, locking and strong coupling effects. *J. Acoust. Soc. Am.* **131**, 1–15 (2012).
68. Zak, J. Berry's phase for energy bands in solids. *Phys. Rev. Lett.* **62**, 2747–2750 (1989).
69. Li, M., Tang, H. X. & Roukes, M. L. Ultra-sensitive nems-based cantilevers for sensing, scanned probe and very high-frequency applications. *Nat. Nanotechnol.* **2**, 114–120 (2007).
70. Ekinci, K., Yang, Y. T. & Roukes, M. Ultimate limits to inertial mass sensing based upon nanoelectromechanical systems. *J. Appl. Phys.* **95**, 2682–2689 (2004).
71. Leeson, D. B. Oscillator phase noise: A 50-year review. *IEEE Trans. Ultrason. Ferroelectr. Freq. Control* **63**, 1208–1225 (2016).

Acknowledgements

J.M.D.P., L.I., R.A. and R.V.C. acknowledge the financial support of the European Union H2020 Future and Emerging Technologies (FET) Proactive Metamaterial Enabled Vibration Energy Harvesting (MetaVEH) project under Grant Agreement No. 952039 in supporting the research activity and the prototype realization. X.Z., T.M., and C.C. were funded by the National Science Foundation (NSF) under grant No. 2034948. Authors acknowledge Prof. Amit Lal and Rohan Sanghvi from Cornell University for access to the Laser Doppler Vibrometer and measurements.

Author contributions

J.M.D.P. and X. Z. contributed equally to the paper; C.C., R.V.C., J.M.D.P., X.Z. and R.A. developed the research plan; J.M.D.P. and L.I. conceived the initial design, the physical concept, and developed analytical and numerical models; X.Z. and C.C. designed, modeled through FEM, and fabricated the device; J.M.D.P., L.I. and R.V.C developed the theory and the physical interpretation; X.Z., T.M., B.D, M.C. and C.C. contributed to the design of experiments; All the authors contributed in writing the paper.

Competing interests

The authors declare no competing interests.

Additional information

Supplementary information The online version contains supplementary material available at <https://doi.org/10.1038/s41467-024-53925-8>.

Correspondence and requests for materials should be addressed to Cristian Cassella.

Peer review information *Nature Communications* thanks Araceli Hernandez Granados and the other anonymous reviewer(s) for their contribution to the peer review of this work. A peer review file is available.

Reprints and permissions information is available at <http://www.nature.com/reprints>

Publisher's note Springer Nature remains neutral with regard to jurisdictional claims in published maps and institutional affiliations.

Open Access This article is licensed under a Creative Commons Attribution-NonCommercial-NoDerivatives 4.0 International License, which permits any non-commercial use, sharing, distribution and reproduction in any medium or format, as long as you give appropriate credit to the original author(s) and the source, provide a link to the Creative Commons licence, and indicate if you modified the licensed material. You do not have permission under this licence to share adapted material derived from this article or parts of it. The images or other third party material in this article are included in the article's Creative Commons licence, unless indicated otherwise in a credit line to the material. If material is not included in the article's Creative Commons licence and your intended use is not permitted by statutory regulation or exceeds the permitted use, you will need to obtain permission directly from the copyright holder. To view a copy of this licence, visit <http://creativecommons.org/licenses/by-nc-nd/4.0/>.

© The Author(s) 2024

Localized Topological States beyond Fano Resonances via Counter-Propagating Wave Mode Conversion in Piezoelectric Microelectromechanical devices: Supplementary Information

Jacopo M. De Ponti^{1*}, Xuanyi Zhao^{2*}, Luca Iorio¹, Tommaso Maggioli², Marco Colangelo², Benyamin Davaji², Raffaele Ardito¹, Richard V. Craster^{3,4}, Cristian Cassella^{2*}

¹ *Dept. of Civil and Environmental Engineering, Politecnico di Milano, Piazza Leonardo da Vinci, 32, 20133 Milano, Italy*

² *Electrical and Computer Engineering Department, Northeastern University, Boston, US*

³ *Department of Mathematics, Imperial College London, London SW7 2AZ, UK*

⁴ *Department of Mechanical Engineering, Imperial College London, London SW7 2AZ, UK*

^{*} *Corresponding Authors: jacopomaria.deponti@polimi.it, zhao.xuan@northeastern.edu*

To aid insight into the underlying physics of the localized topological states via counter-propagating wave mode conversion, we provide a detailed description of the analytical and numerical models we have developed to investigate the theory presented in the main manuscript. The list of symbols used in the main manuscript and in the supplementary information are given in Table S1.

ANALYTICAL MODEL

An analytical toy model has been devised to simplify the complex real structure and its behaviour in wave mechanics. The simplest model that can fully describe counter-propagating wave mode conversion, usually named as wave locking [1], is a double bi-atomic

chain where the mode of first chain is forced to interact with the mode of the second chain through a periodic coupling which is given, in the simplest case, by elastic springs.

As reported in the main text, the two infinite chains are analytically defined by imposing Bloch-Floquet boundary conditions to the bi-atomic system. The non-perturbed Hamiltonian for the single bi-atomic chain is:

$$\hat{H}_\kappa = \begin{bmatrix} (k_1 + k_2)/m_1 & -(k_1 + k_2 e^{i\kappa})/m_1 \\ -(k_1 + k_2 e^{-i\kappa})/m_2 & (k_1 + k_2)/m_2 \end{bmatrix} \quad (S1)$$

where m_1 and m_2 are the particle masses, k_1 and k_2 the stiffnesses and κ the wavenumber that goes from $-\pi/a$ to π/a , being a the lattice constant. In order to define the solution for two non-interacting chains, the total Hamiltonian of the system reads:

$$\hat{H}_\kappa = \begin{bmatrix} (k_1 + k_2)/m_1 & -(k_1 + k_2 e^{i\kappa})/m_1 & 0 & 0 \\ -(k_1 + k_2 e^{-i\kappa})/m_2 & (k_1 + k_2)/m_2 & 0 & 0 \\ 0 & 0 & (k_3 + k_4)/m_3 & -(k_3 + k_4 e^{i\kappa})/m_3 \\ 0 & 0 & -(k_3 + k_4 e^{-i\kappa})/m_4 & (k_3 + k_4)/m_4 \end{bmatrix} \quad (S2)$$

By introducing this Hamiltonian into the time-independent Schrödinger equation (eq. (1) in the main manuscript), and imposing Bloch-Floquet boundary conditions, we obtain the dispersion relation in Fig. 2-b of the main manuscript, where band crossing is observed. To introduce wave coupling between the two chains, a perturbation of the original Hamiltonian \hat{H}_κ is defined as $\hat{H}_\kappa^{tot} = \hat{H}_\kappa + \hat{H}'$, with \hat{H}' equal to:

$$\hat{H}' = \begin{bmatrix} s/m_1 & 0 & -s/m_1 & 0 \\ 0 & s/m_2 & 0 & -s/m_2 \\ -s/m_3 & 0 & s/m_3 & 0 \\ 0 & -s/m_4 & 0 & s/m_4 \end{bmatrix}, \quad (S3)$$

This solution considers now a coupling spring attached

to each mass of the bi-atomic chain, allowing for energy flow from one chain to the other. The corresponding dispersion curves are reported in Fig. 2-d of the main manuscript, where a complete bandgap appears due to the coupling of the two states. Table S2 reports the parameters used for the analytical results reported in the main manuscript.

To investigate the topological features of this bandgap, we then calculate the Zak phase [2] for two chains, named as C1 and C1', having stiffness k_1-k_2 , k_3-k_4 and its mirrored counterpart k_2-k_1 , k_4-k_3 , respectively. This calculation, allows us to verify that, if an interface is encountered between cells C1 and C1', non trivial interface states localized at the common interface exist, and these states are topologically protected, being the bandgaps of C1 and

Symbol	Definition
a	Unit cell size.
Δ	Distance between the plate surface corrugations.
f_1	Frequency of the first topological state.
f_2	Frequency of the second topological state.
f_3	Frequency of the destructive interference between topological states.
κ	Wavenumber.
k_1, k_2, k_3, k_4	Springs in the spring-mass model.
m_1, m_2, m_3, m_4	Masses in the spring-mass model.
τ	Normalised transmission spectrum.
ω	Angular frequency.
ω_t	Maximum angular frequency of the dispersion curve above the topological bandgap.
Ω_1	Normalized angular frequency of the first topological state (L-infinity norm).
Ω_2	Normalized angular frequency of the second topological state (L-infinity norm).
S_{21}	Scattering parameter, i.e. voltage ratio between ports $S_{21} = 20 \log_{10}(V_2/V_1)$.
Q	Quality factor.
Q_{al}	Quality factor associated to anchor losses.
φ^{Zak}	Zak phase.

TABLE S1. Table of symbols

Variable	Value
m_1, m_2, m_3, m_4	1, 1, 5, 5
k_1, k_2, k_3, k_4	1, 1.2, 0.8, 2
s	0.5
a	1

TABLE S2. Parameters used in the analytical spring-mass model of Fig.3.

C1' endowed with distinct Zak phases. The Zak phase, φ_n^{Zak} , for the n^{th} band is defined in terms of the Berry connection $\chi(\boldsymbol{\kappa})$ such that

$$\varphi_n^{Zak} = \int_{-\pi/a}^{\pi/a} \chi(\boldsymbol{\kappa}) d\boldsymbol{\kappa} = i \int_{-\pi/a}^{\pi/a} \langle \psi_n(\boldsymbol{\kappa}) | \partial_{\boldsymbol{\kappa}} \psi_n(\boldsymbol{\kappa}) \rangle d\boldsymbol{\kappa}, \quad (\text{S4})$$

where a is the lattice constant, $\partial_{\boldsymbol{\kappa}}$ is the partial derivative with respect to the wavevector $\boldsymbol{\kappa}$ and $\psi(\boldsymbol{\kappa})$ is the eigensolution for the n^{th} band. Since a straightforward implementation of perturbation theory cannot provide the Zak phase as a loop integral of the connection, we implement the more general discrete approach without assuming any regularity of the phase along the path [3]:

$$\varphi_n^{Zak} = -\Im \left(\log \prod_{s=1}^N \langle \psi_n(\boldsymbol{\kappa}_s) | \psi_n(\boldsymbol{\kappa}_{s+1}) \rangle \right). \quad (\text{S5})$$

In Eq. (S5) the periodic gauge condition is satisfied through Bloch condition $|\psi_n(\boldsymbol{\kappa}_{N+1})\rangle = e^{-i\mathbf{G}\cdot\mathbf{r}}|\psi_n(\boldsymbol{\kappa}_1)\rangle$, being \mathbf{G} and \mathbf{r} the reciprocal and Bravais lattice vectors respectively.

Due to the intrinsic connection with Wannier charge centers [4, 5], provided that we have inversion symmetry with respect to the array axis, the Zak phase can

only assume two values: 0 or π . We find distinct Zak phases for all the branches of C1 and C1'. As such, we have an analogue of an incomplete Wannier state at the interface between C1 and C1'. This state supports topological interface states. The values of the Zak phases for each dispersion branch are reported Fig. 2-d of the main manuscript.

The existence of the two states is also corroborated performing a supercell dispersion analysis, i.e. considering a long chain having an interface between C1 and C1'; the two interface states, with mixed out-of-plane and in-plane polarization, are shown in Fig. 2-d of the main manuscript. We can also numerically investigate the origin of State-3. In this regard, the interference between State-1 and State-2 is analytically demonstrated by analyzing in frequency domain two coupled chains with an interface, as shown in Fig. S1-a. Computing the transmission τ (Fig. S1-b) between two degrees of freedom close to the interface allows to identify two states at the normalized frequencies Ω_1 and Ω_2 that correspond to States-1,2 of our MEMS device. τ also shows the presence of an interference state at a normalized frequency Ω_3 that corresponds to State-3 in our MEMS device. Finally, our numerical investigation further demonstrates the stronger localization that the system in Fig. S1-a shows at Ω_3 compared to both Ω_1 and Ω_2 ((Fig. S1-c)).

NUMERICAL ANALYSES

Numerical analysis are performed using both ABAQUS[®] and COMSOL[®] FEM software.

To corroborate the existence of the two interface states, we complement the numerical dispersion analyses with a two-dimensional (2D) spatiotemporal Fast Fourier Transform (FFT) of the wavefield obtained from our time do-

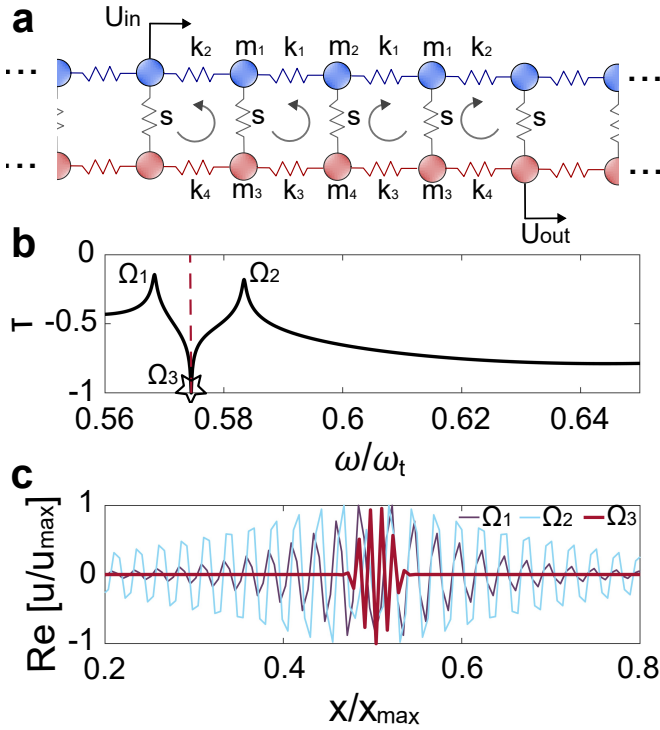


FIG. S1. (a) Two coupled spring mass chains with an interface are used to predict the two interface states and their destructive interference. (b) Analytical transmission computed as the ratio between the displacement of two degrees of freedom close to the interference, named as U_{in} and U_{out} . (c) Stronger wave localization is observed at Ω_3 compared to both Ω_1 and Ω_2

main analyses performed in ABAQUS®. We adopt a Finite Element discretisation based on 8-node biquadratic plane strain quadrilateral elements (CPE8), with 2 degrees of freedom (dof) for each node. The analysis is per-

formed via implicit time integration based on the Hilber-Hughes-Taylor operator [6], an extension of the Newmark β -method with a constant time increment $dt = 1 \text{ ns}$. We consider a system with an SSH interface, 10 cells on each side and external absorbing boundary conditions using the ALID (Absorbing Layers using Increasing Damping) method [7]. The system is excited through an imposed vertical force at the interface, using a linear finite chirp from 40 to 120 MHz with a tapered cosine window and time duration of $1 \mu\text{s}$. The wavefield, measured in a spatial domain close to the interface, is then 2D Fast Fourier Transformed in order to get the spectrogram reported in Fig. 1(d) of the main manuscript.

REFERENCES

- [1] B. R. Mace and E. Manconi, Wave motion and dispersion phenomena: Veering, locking and strong coupling effects, *J. Acoust. Soc. Am.* **131**, 1015 (2012).
- [2] J. Zak, Berrys phase for energy bands in solids, *Phys. Rev. Lett.* **62**, 2747 (1989).
- [3] R. Resta, Manifestations of Berry's phase in molecules and condensed matter, *J.Phys.: Condens. Matter* **12**, 107 (2000).
- [4] W. Kohn, Analytic properties of Bloch waves and Wannier functions, *Phys. Rev.* **115**, 809 (1959).
- [5] S. Kivelson, Wannier functions in one-dimensional disordered systems: Application to fractionally charged solitons, *Phys. Rev. B* **26**, 4269 (1982).
- [6] H. M. Hilber, T. J. R. Hughes, and R. L. Taylor, Improved numerical dissipation for time integration algorithms in structural dynamics, *Earthq. Eng. Struct. Dyn.* **5**, 283–292 (1977).
- [7] P. Rajagopal, M. Drozd, E. A. Skelton, M. J. Lowe, and R. V. Craster, On the use of absorbing layers to simulate the propagation of elastic waves in unbounded isotropic media using commercially available finite element packages, *NDT & E International* **51**, 30 (2012).